The Effects of Layer Thickness on Brittle Boudinage in 3D

Bob Bamberg[a,1]*, Christoph von Hagke[a,2], Simon Virgo[a,3], Janos L. Urai[a]

[a] Structural Geology, Tectonics and Geomechanics, RWTH Aachen University, Lochnerstrasse 4-20, 52056 Aachen, Germany

Now at

[1] School of Geology, Geography and the Environment, University of Leicester, University Road, Leicester LE1 7RH, United Kingdom
[2] Department of Geography and Geology, Salzburg University, Hellbrunnerstraße 34, 5020 Salzburg, Austria
[3] Terranigma Solutions GmbH, Laurentiusstrasse 59, 52072 Aachen, Germany

Contact details

B. Bamberg: bobbamberg@gmail.com (corresponding author)
C. von Hagke: christoph.vonhagke@plus.ac.at
S. Virgo: simon@terranigma-solutions.com
J.L. Urai: janos.urai@geostructures.nl

Keywords

boudinage, fracture spacing, brittle, 3D, tomography, strain analysis

This manuscript has been submitted for peer review to the **'Advances in Modern Structural Geology: A special issue in honour of the life and work of John G. Ramsay'** of the **Journal of Structural Geology**.

The Effects of Layer Thickness on Brittle Boudinage in 3D

Bob Bamberg[a,1]*, Christoph von Hagke[a,2], Simon Virgo[a,3], Janos L. Urai[a]

[a]Structural Geology, Tectonics and Geomechanics, RWTH Aachen University, Lochnerstrasse 4-20, 52056 Aachen, Germany
[1] School of Geology, Geography and the Environment, University of Leicester, University Road, Leicester LE1 7RH, United Kingdom
[2] Department of Geography and Geology, Salzburg University, Hellbrunnerstraße 34, 5020 Salzburg, Austria
[3] Terranigma Solutions GmbH, Laurentiusstrasse 59, 52072 Aachen, Germany

*corresponding author: bobbamberg@gmail.com

Keywords: boudinage, fracture spacing, brittle, 3D, tomography, strain analysis

Abstract

We analyse the effects of thickness on brittle boudinage in a metre-scale sample of marble containing a layer of amphibolite recording two phases of ductile pinch-and-swell followed by five generations of brittle boudinage. The amphibolite geometry was reconstructed in 3D, employing a method we call 'outcrop-scale tomography'. Our data suggests that strain localisation depends on the ration of grain size and layer thickness of amphibolite. In very thin layers (few grains across), strain is diffuse throughout the entire layer, leading to macroscopically homogeneous stretching. Strain localisation increases when layer thickness is more than 10 grains, first through narrow tensile necks and shear zones (<10-20x average grain size), then through extension fractures, and finally shear fractures emerge. The disappearance of shear fractures in thinner layers can be explained by a geometry-related compressive stress decrease in the pinches and expected shear band width exceeding layer thickness. This results in localized shear evolving only in thicker layers. Successive reactivation between fracture generations, geometrical complexity, in the form of splays and branches, and the thickness-dependence of localised strain govern fracture distribution in the layer. We infer a second, temporal trend that records the progressive embrittlement of the rocks as they cool during exhumation, evidenced by a switch from shear to extensional fracturing. In the final stages, the marble is brittle enough to allow fracture propagation from the amphibolite across the material interface and the formation of throughgoing brittle faults.

1 Introduction

Boudinage is the periodic failure – brittle or ductile – of competent layers in a mechanically-layered material under coupled layer-parallel extension *(e.g. Ramberg, 1955)*. Boudins provide a rich archive to untangle the deformation history in the mechanically layered crust. First, boudins occur on all scales, from crustal-scale extension forming island chains *(Jolivet et al., 2004)*, down to boudinage of microscopic, brittle grains in ductile rocks. Second, their geometry depends on paleo-rheology and strain rate *(Ramberg, 1955, Ramsay, 1968, Ramsay & Huber, 1983, 1987)*. The importance of boudins for understanding deformation histories, as well as their geometric variability has been appreciated since more than hundred years *(Ramsay, 1881, Lohest, 1909, Ramberg, 1955, Ramsay, 1968, Ramsay & Huber, 1983, 1987)*. A unifying taxonomy has been proposed by Goscombe et al. *(2004)*, who subdivide boudins into five end members, in particular: ductile drawn boudins (formerly pinch-and-swell), brittle torn boudins separated by extensional fractures, bookshelf-rotated domino boudins separated by straight antithetic shear fractures, or gash boudins separated by sigmoidal or forked shear veins and fractures, and finally shearband boudins resulting from synthetic

shearing. Our understanding of the mechanisms controlling boudinage and the resulting geometries has greatly improved in the past two decades, especially through the use of analogue and numerical modelling. Analogue models *(Zulauf & Zulauf, 2005, Zulauf et al., 2020a, b)* and numerical models *(Abe et al., 2013, Virgo et al., 2013, Virgo et al., 2014, Virgo et al., 2016)* reveal how complex boudin interference structures can evolve from multiphase and/or high-strain deformation. Numerical models have also shown to be a valuable tool in exploring the rheological control on boudin geometry and internal stress distribution *(Bai et al., 2000, Schmalholz et al., 2008, Schöpfer et al., 2011, Abe & Urai, 2012, Schöpfer et al., 2017)*. Nevertheless, we still do not fully understand the mechanics of boudin formation, especially the factors controlling boudin localisation. In this study we build on data presented in Von Hagke et al. *(2018)* to expand on the role of structural inheritance and the effects of layer thickness in particular, on brittle boudin geometry and failure mode. Our data reveals three surprising effects: boudin width is not, or only weakly controlled by layer thickness, and fracture mode as well as brittly resolved extension are proportional to layer thickness.

Brittle boudins evolve through sequential fracture infilling, i.e. fractures forming in between existing fractures, until the fractures are saturated and a steady-state boudin width is reached, which is generally defined by layer thickness *(Ramberg, 1955, Price, 1966, Mandal et al., 1994, Bai et al., 2000, Schöpfer et al., 2011, Marques et al., 2012)*. Geometrical complexity such as splay and fractures clustering in arrays *(Olson, 2004, Abe & Urai, 2012)* develops during this early stage of infilling, while maximum tensile stress is still heterogeneously distributed along the layer *(Schöpfer et al., 2011)*. Once saturation is reached, fracture density should correlate directly with material rheology and stress state in the competent layer *(Bai & Pollard, 2000b, Schöpfer et al., 2011, Zulauf et al., 2020a)*. When coupling between matrix and competent layer is relatively strong compared to the layer's tensile strength, interfacial slip is suppressed, and a zone of compressive layer-parallel stress will develop centrally inside the boudins once they reach a critical aspect ratio of about 1. At this stage, further boudin segmentation is only possible through additional weakening factors such as material defects or elevated fluid pressure *(Bai et al., 2000, Bai & Pollard, 2000b, Schöpfer et al., 2011)*.

In order to reconstruct the full deformation history recorded in boudin structures it is crucial to investigate their geometry in all three dimensions, as only sectional and map views combined can reveal the full complexity of boudin structures *(Zulauf & Zulauf, 2005, Zulauf et al., 2011, Marques et al., 2012, Abe et al., 2013, Virgo et al., 2018, Von Hagke et al., 2018, Zulauf et al., 2020a)*. 3D boudin analysis has shown that identifying multistage deformation with the same failure mode is in general not possible from a 2D section alone *(Virgo et al., 2018, Von Hagke et al., 2018)*. Similarly, tablet boudins formed either in one episode of pure flattening *(Zulauf et al., 2011)*, in nonplane strain *(Abe et al., 2013)*, or through polyphase deformation during rotating plane strain *(Zulauf et al., 2014)* look identical in sections but reveal their deformation history in map view. Finite strain can also be underestimated when secondary reworking of boudins that have been parallelised to the extension axis by in-plane folding goes unnoticed *(Zulauf & Zulauf, 2005, Zulauf et al., 2020a)*.

We present data from serial sectioning of a mined, wedge-shaped marble block with a height of 37 cm and face lengths of 250, 224, and 140 cm *(Fig. 1 in Von Hagke et al., 2018)*. It contains a single boudinaged amphibolite layer with variable thickness resulting from an earlier ductile pinch-and-swell boudinage, cut by brittle boudins with axes subnormal to the pinch-and-swell structure. It was recovered from the marble mine south of Kinidaros on Naxos island, Greece (37°05'12.6" N, 25°28'20.0" E), where a large marble raft from the high-strain zone subdividing the migmatite dome is cropping out. The in-situ orientation of the block is not completely known, but can be reconstructed by comparing the boudin structures to the field data from Virgo et al. *(2018)*: the amphibolite layer had to be vertical and striking N-S.

2 Geological Background

The island of Naxos, in the centre of the Aegean Sea, offers a unique opportunity to study multiphase boudinage structures in three dimensions. Marbles, mined for their clear white colour and large crystal size, are intercalated with centimetre to decimetre thick amphibolite and pegmatite layers, and have undergone multiphase deformation *(Schenk et al., 2007, Virgo et al., 2018)*. Naxos is a metamorphic core complex exhumed by a crustal-scale, N-dipping detachment with top-to-the-N sense of shear *(Lister et al., 1984, Urai*

et al., 1990). Extensional tectonics in the back-arc basin are a manifestation of slab rollback following southward migration of early Alpine subduction in the Hellenic arc *(Fytikas et al., 1984, Jolivet & Brun, 2010, Jolivet et al., 2013)*. The metamorphic core complex hosts a central migmatite dome subdivided in three sub-domes, with several marble enclaves and rafts in and around the high-strain zone separating the southern from the central sub-dome *(Vanderhaeghe, 2004, Kruckenberg et al., 2011)*. Deformation structures in these marble rafts indicate multiphase E-W shortening evidenced by two sets of ductile pinch-and-swell boudinage, isoclinal folding and 5 sets of brittle boudinage in the amphibolite layers *(Virgo et al., 2018, Von Hagke et al., 2018)*. The pegmatites, which intruded the marble after ductile deformation in the amphibolite, only display 2 sets of brittle boudinage *(Schenk et al., 2007)*. The structures within the marble rafts are thought to post-date development of similar coupled folding and boudinage in the metasediments surrounding the migmatite dome *(Urai et al., 1990, Buick, 1991, Virgo et al., 2018)*.

3 Sample & Methods

We employed 'outcrop-scale tomography' *(Von Hagke et al., 2018)* to generate a 3D model of the boudin train. The internal structure of the metre-sized sample is reconstructed from centimetre thin slices cut using an industrial diamond saw. The sample was cut perpendicular to the axes of brittle boudins, as interpreted in the field. The slabs are about 2 cm thick, with a kerf loss of about 1 cm. Both faces of the slabs were digitised using a Nikon D800 camera with a Nikkor Micro 60 mm f/2.8D lens, resulting in an image resolution of 0.2 mm/pixel and negligible distortion of 1 mm over a frame width of 1450 mm. The boudin structure was then reconstructed from the spatially referenced images in Midland Valley's (now Petroleum Experts) Move 2016 suite. In each slice (i.e. image), we mapped fault traces (classified according to failure mode), layer top and bottom, inter-boudin width (measuring dilatancy), and then correlated these across slices (Figure 1). Thus, 5087 fracture traces created a 3D network of 841 fractures planes. Details of the interpretation were verified by dissolving the marble in selected slabs using hydrochloric acid. Photogrammetry models of thus exposed amphibolite were integrated into the model and confirmed our interpretation. The effects of thickness on fracture spacing, failure mode and resolved strain are quantitatively analysed in synthetic sections calculated from the 3D model and striking perpendicular to the thickness gradient of the amphibolite layer (4° clockwise misorientation to the slices, Figure 1A). Microstructural analysis was performed using the Petroscan Virtual microscope *(Virgo et al., 2016)*.

4 Results

In the following we show our observation in the reference frame of the sample, with the amphibolite layer horizontal. Orientations in this reference frame are indicated by an asterisk. We note that the amphibolite layer was oriented sub-vertically with the E-W* axis trending N-S, as explained above.

4.1 Observed Structures

The amphibolite layer's thickness varies across the older drawn boudin. Drawn boudins are present in two generations, and the older long wavelength (lλ) boudins are responsible for the metre-scale thickness gradient from the long end to the short end of the sample *(Virgo et al., 2018)*. Their wavelength exceeds the sample width, probably around 2-3 m. The second generation (sλ) has a wavelength of ca. 10-20 cm and is only developed in the pinches of lλ boudins (Figure 1A).

Drawn boudins are overprinted by at least 5 sets of brittle boudinage. They are described in detail in Von Hagke et al. *(2018)*, and summarised in (Figure 2). From oldest to youngest, they are:

NW*: Straight continuous torn boudins with-millimetre aperture, striking 122 ± 9.2°*, 24 planes. Owing to their minimal aperture, they are only sparsely identified and mapped in the 3D model, but are easily identified in etched samples *(Von Hagke et al., 2018)*.

NNW*: Torn - domino boudins striking 157 ± 14.2°*, 142 planes. Fracture planes dip 247/83°* on average, with minimal throw and aperture below 1 mm.

NNE*: Domino boudins striking 5 ± 15°*, 168 planes. Fracture planes dip 275/60°* on average, with throws generally within 1.2 - 17.5 mm, but reaching up to 30 mm and an aperture of up to 3 mm.

N*: Torn boudins with apertures up to 3 mm striking 178 ± 15°*, 417 planes. They are the most abundant fractures in the block.

Veins: Chlorite filled veins striking 18 ± 14°*, frequency not recorded as they often don't form continuous planes in layer-normal direction. They are consistently protruding into the marble (i.e. thicker mechanical unit), have an aperture of 1 - 2 mm, a layer-normal length of 2 - 5 cm and a consistent spacing of 5 – 10 cm. In thick amphibolite they tend to be pinned to older, well-developed fractures.

Chlorite slickenfibres developed in many sheared inter-boudin zones, recording sense of motion, dilatancy, and periodicity of deformation. Shear motion is pure dip-slip, with commonly a small extensional component (i.e. hybrid fractures). Reactivation as extensional fractures is frequent and evidenced by ruptured or new slickenfibres. Both shear and extensional fractures are reactivated by chlorite veins in inter-boudin zones and layer-normal chlorite veins above and below shear fractures in the marble. The different fracture sets are also strongly interconnected, with frequent bridging or reactivation and extension of older fractures by younger ones. Interaction between the NNW*, NNE* and N* sets is almost exclusively characterised by Y-nodes, suggesting that newly developed fractures readily propagate towards and merge with existing fractures.

4.2 Effects of Thickness

The large-scale thickness variation of the amphibolite layer originating from early drawn boudinage provides an opportunity to investigate the effect of layer thickness in brittle boudinage. Other potential controls on boudin geometry like the amphibolite's mechanical properties, grain size, deformation history as well as external factors like far-field stress (and hence marble flow) can be assumed to remain constant within the sample, leaving amphibolite thickness as the only major variable. Fracture geometry and distribution reveal three parameters correlating with layer thickness: fracture distribution, failure mode, and macroscopically resolved extension.

4.2.1 Fracture Spacing

Boudin widths in the model, (i.e. fracture spacing) can be analysed using two methods. The more intuitive approach is to count fracture intersections along sections normal to the thickness gradient (referred to as top-down). This has the advantage that we can calculate the spacing for each boudin generation. However, the results might be biased through errors in interpolation and classification as well as reactivation of older fractures, preventing the formation of some fractures. These drawbacks can be circumnavigated by the second approach, where we only count observed fractures in the physical slabs (bottom-up in the following). This, however, oversimplifies the system as it does not account for strain field rotation between different boudin generations forcing new localisation instead of reactivation of older fractures. Also, the approach might overestimate fracture density where fractures interact or splay. Finally, since fracture orientation is unknown and changes from fracture to fracture, we cannot correct the calculated spacing for the length-overestimation resulting from measuring on non-orthogonal sections. The resulting overestimation of spacing is significant only for the low-density NW* set (88.7 %) but acceptable for all other sets (NNW*: 8.6 %, NNE*: 0.4 %, N*: 0.1 %, Veins: 5.1 %).

Results from both approaches are very similar for extensional fractures but less so for shear fractures (Figure 3). NNE* shear fracture spacing (top-down) follows a negative power-law correlation to thickness with an exponent of -0.8 ± 0.11 and an R^2 of 0.6. Conversely, shear fracture spacing in the bottom-up approach shows a positive linear or power-law correlation to thickness, like N* fractures in the top-down approach, and both extension and all mapped fractures in the bottom-up approach. Fitting parameters are summarised in Table 1. Extensional fracture spacing (N* in top-down and extensional in bottom-up) might not correlate to layer thickness at all as R^2 for both fits are < 0.1. The high variance of fracture spacing measured in subsets of fractures (i.e. NNE*, N*, shear, or extensional fractures) is significantly reduced if data for shear and extensional fractures are summed up to calculate overall fracture spacing (3144 & 5441 vs 467, respectively). This may mean that there is significant reactivation. This is also evident in Figure 3C, where fracture spacing and amphibolite thickness are plotted along the thickness gradient. The plot reveals a striking

negative spatial correlation between the two dominant fracture sets in the sample, N* (extensional) and NNE* (shear) fractures. N* fractures preferentially develop in areas with less pre-existing (NNE*) fractures. The trend also shows a rather distinct nonlinearity, not related to any measurable thickness variation. Averaging spacing yields a much less variable trend, highlighting how reactivation is an effective way to suppress further fracture nucleation where fracture density is high *(Passchier et al., 2021, Prabhakaran et al., 2021a, Prabhakaran et al., 2021b)*.

4.2.2 Failure Mode

Extension in the amphibolite layer is dominantly accommodated by slip of shear fractures where the layer is thick, as opposed to dilatancy of extensional fractures where it is thin (Figure 4A). This observation is corroborated by the dip vs thickness (Figure 4B) and extension vs thickness data (Figure 4C), both showing positive correlations. Dip angles of the NNE* and NNW* sets, which both have a distinct shear component, display a very similar negative correlation to thickness with an average factor of about -0.35°/mm. The purely extensional N* and NW* sets' dip angles remain largely constant over the entire thickness range. Dip angles are used as proxies for the failure mode, with the underlying assumption that extensional fractures should develop at ca. 90° to the layer interface and this angle decreases as the shear component of deformation increases.

4.2.3 Brittle Extension

Extension localized in brittle boudinage is either accommodated by purely layer parallel dilatancy or by heave, the layer parallel component of shear slip. Slickenfibres in the etched blocks confirm the movement between boudins to be pure dip-slip. Dilatancy and heave, both normalised to finite boudin train length, can easily be extracted from the 3D model *(see Von Hagke et al., 2018)* and provide a direct approximation of finite strain accommodated by brittle boudinage (Figure 4C). While dilatancy is essentially thickness invariant, heave is correlated related to thickness. As a result, their sum, total brittle extension also correlates to layer thickness, ranging from ca. 5 % at 5 mm to 16 % at 32 mm. Notably, the linear fit for heave suggests a lower threshold for the development of shear fracturing around 10 mm thickness. Further, dilatancy below this thickness is exclusively accommodated by chlorite veins, which are controlled by a different mechanical unit (they extend into the marble) as the previous boudin generations. Hence, we can consider 10 mm to be the threshold below which no fractures localise in our sample, and indeed, unless linked to a chlorite vein, we can observe deformation progressively delocalising below 10 mm layer thickness (Figure 5A). This correlation between fracturing and thickness is also reflected in failure mode and fracture spacing, notably the negative power-law trend of the NNE* set (Figure 3A).

4.3 Microstructure

Thin sections from thick and thin amphibolite show similar grain size distribution (plagioclase: 0.2 - 0.5 mm, amphibole: 0.3 – 1 mm), degree of crystal plastic deformation, and frequency of grain cracking. Only two differences are apparent: The concentration of calcite and deformation bands. While calcite is absent in thick amphibolite, small, disseminated pockets of up to few hundred micrometres across become more common where the layer thins. Distributed microscopic strain is accommodated by deformation bands across the thickness range (Figure 5B-E). They are characterised by consistent alignment of grain boundaries, concentration of small, rounded grains, biotite, and chlorite along the aligned boundaries, as well as occasional intragranular deformation, either as slip along cleavage planes, asperity removal, or crystal plastic deformation. When abutting against larger grains, deformation bands can bifurcate around the grain and reunite, or splay and continue as multiple bands. Less frequently in the amphibolite, but commonly in the coarser marble, they penetrate and terminate within a grain. Where identifiable, displacement on these bands does not exceed a few micrometres. These deformation bands are abundant throughout the whole layer in thick amphibolite, irrespective of proximity to fractures, whereas in thinner amphibolite they are only abundant in and around macroscopically identifiable sites of deformation, be they fairly localised shear bands or less localised necks. As such, they are another manifestation of brittle strain decreasing with layer thickness.

5 Discussion

5.1 Spacing

Due to the thickness variation from old drawn boudins, our sample block provides a unique opportunity to evaluate the effects of layer thickness on boudinage. Results show a clear relationship between thickness and failure mode (Figure 4) as well as total brittle extension as measured by offset fractures (Figure 4C). On the other hand, the relationship between layer thickness and fracture spacing is far more ambiguous as would be expected from previous studies *(e.g. Mandal et al., 1994, Bai et al., 2000, Schöpfer et al., 2011, Marques et al., 2012)*. Fracture spacing in the individual sets shows only weak correlation to thickness in the case of the NNE* set, but not the N* set (Figure 3A). Moreover, spacing of NNE* fractures correlates negatively with thickness, in stark disagreement to all the previous work which assume that strain is distributed homogeneously through the boudinaged layer. The negative trend is, however, consistent with resolved strain increasing with layer thickness. The high variance in spacing of both NNE* and N* sets, and thus the weak correlation, can partly be explained by complex fracture geometries with abundant splaying and branching, as well as reactivation of pre-existing fractures being favoured in the already saturated parts of the layer. Significant reactivation can be expected for the low misorientation between the NNE* and the N* set, especially given the potentially high rheological contrast between soft marble and strong amphibolite *(Virgo et al., 2014)*. Also, assuming a fracture infill model *(Bai et al., 2000, Bai & Pollard, 2000a, Bai & Pollard, 2000b)*, new fracture nucleation stops as boudin aspect ratio approaches 1 and additional strain is accommodated in the inter-boudin zones (i.e., by the fractures in our case). The significance of structural inheritance becomes evident when plotting spacing along a thickness section through the amphibolite (Figure 3C), showing the alternating dominance of either the older NNE* or the younger N* set, while the average combined spacing stays relatively constant. This supports the assumption that NNE* fractures are reactivated during the subsequent N* deformation, and new fractures only develop where the former are scarce. The considerably lower variance of fracture spacing across all sets (Figure 3B) compared to individual fracture generations (Figure 3A) further supports this hypothesis. Extensional fracture spacing shows no significant correlation to thickness, and spacing between shear fractures as well as between all fractures, not distinguished between fracture modes or sets, follows a low-exponent power law or linear trend. The boudin aspect ratio of only about 0.3 is significantly lower than the critical aspect ratio expected from the fracture infill model *(Bai et al., 2000, Schöpfer et al., 2011)*. The low fracture spacing in our model is related to splay and fracture clustering, which evolve during the infill phase of fracturing when maximum tensile stress is not yet bound to the boudin centre *(Schöpfer et al., 2011)*. Our data support a weak link between fracture spacing and layer thickness, but other factors such as structural inheritance and geometrical complexity arising from fracture nucleation and propagation are occluding any potential strong correlation to thickness.

5.2 Failure Mode

The variation in strain accommodated by brittle fractures - shear or extensional - can be explained by differential embrittlement during uplift and cooling, and the geometrical constraints on failure mode following pinch-and-swell boudinage. Fracture concentration increases in each consecutive fracture set (Figure 2), indicating progressive embrittlement of both amphibolite and marble at different rates, as well as a decreasing rheological contrast *(Zulauf et al., 2020a, b)*. This confirms the continuous trend of cooling and uplift proposed in Virgo et al. *(2018)*. As a consequence, earlier localisation is more likely to develop as shear fractures (NNW* and NNE* sets) under the higher overburden, while the later N* and vein sets develop as extensional opening mode fractures *(e.g. Schöpfer et al., 2007, Abe & Urai, 2012, Kettermann & Urai, 2015)*. This could be explained by the increased viscosity of the marble limiting material flow around fractures *(Schueller et al., 2005)*, preventing significant block rotation from shear fracturing. A reduced overburden stress could also explain why the chlorite veins protrude into the marble, as they could propagate into the relatively embrittled marble after nucleating in the more competent amphibolite. The precipitation of chlorite veins also evidences the presence of fluids, reducing effective stress in the amphibolite and surrounding marble and thus promoting tensional failure and propagation in the marble *(see also Schenk et al., 2007)*. Further, shear fractures in our sample preferentially localise in the swells (Figure 4), initially in the low-aspect-ratio swell in the N* of the layer (see NNW* set, Figure 2), and later also in the other, higher aspect ratio swells (NNE* set, Figure 2). Mandal et al. *(2001)* demonstrate how tensile stress in brittle inclusions increases linearly with their aspect

ratio, while compressive stress decreases, making low aspect ratio swells more likely to fail in shear while the high aspect ratio pinches fail in tension.

5.3 Strain

The asymptotic increase of fracture spacing for NNE* shear fractures in thinner amphibolite (Figure 3A) is emphasising how thinner rock cannot accommodate shear fractures, but the 'missing' strain is seemingly not transferred to extensional fractures either. The same trend is apparent in the rotation of fracture dip in the shear dominated NNW* and NNE* sets towards layer normal extensional fractures in thinner amphibolite, while the tensile-dominated N* and NW* sets are thickness invariant (Figure 4B). The gradual change in orientation is distinct from the sudden changes in orientation and failure mode resulting from lateral fracture propagation by reactivation. The correlation between brittly resolved strain and thickness is further corroborated by measured macroscopic extension (Figure 4C). Correlation of brittle extension to thickness can mainly be ascribed to the behaviour of shear fractures (Figure 4C). However, local strain variations on the order of 10% are hard to reconcile with overall homogeneous stretching of the marble at the sample scale (ca. 4.5 m^2). Since below 10 mm layer thickness only chlorite veins disrupt the layer, we infer that layer-bound brittle deformation is replaced by macroscopically ductile deformation (Figure 6). This transition to macroscopically ductile deformation in thin layers can also be seen in field data from Naxos, where adjacent layers of different thickness have very different fracture densities and associated macroscopic brittle extension. Fig. 7 in Virgo et al. *(2018)* and Fig. 4 in Schenk et al. *(2007)* show examples of thin amphibolite layers following the stepped post-deformation layer-matrix interface of thicker neighbouring amphibolite or pegmatite layers. The thin sidekick layers must accommodate even more strain than their thicker neighbours, but show no macroscopically localised deformation. Consequently, these layers must accommodate extension by distributed ductile processes as overall fracture density decreases (i.e. spacing increases). Below a thickness of ca. 10 mm brittle deformation is limited to the chlorite veins, which are however not constrained to the amphibolite layer and are most likely controlled by a thicker mechanical unit including the light marble directly adjacent to the amphibolite (Figure 1B). Just below the thickness threshold for brittle localisation, deformation can still 'localise' in cm-wide zones that manifest macroscopically by necking, but without separation. Microscopically, these zones contain a high density of deformation bands (Figure 5), mostly following and aligning grain boundaries. However, these bands are much more abundant in thicker amphibolite, where they are not limited to the vicinity of fractures but are also common in boudin centres (Figure 5E). Also, the deformation mechanism governing these bands remains elusive. They show neither evidence of cataclasis, compaction, nor mineral alteration. Their distribution suggests that distributed brittle strain is also proportional to layer thickness, consequently these bands are not accommodating 'missing' extension in the pinches. Increased concentration of calcite in thin amphibolite could indicate intergranular fracturing and subsequent granular flow as a possible mechanism for distributed deformation, as described for the pinch-and-swell boudins by Virgo et al. *(2018)*. However, to preserve the high grain angularity seen in the amphibolite, considerable dilatation would have been necessary, which would require a fluid pressure that should manifest in much more significant mineralisation *(Stel, 1981)*. The absence of layer-bound fractures in very thin amphibolite is possibly an effect of intergranular fracturing *(Abe & Urai, 2012, Virgo et al., 2018, Spruženiece et al., 2021)* saturating the layer before cracks can coalesce into localised fractures. This is not surprising considering that the layer is less than 10 – 20 grains across, well below the expected shear band thickness *(e.g. Mühlhaus & Vardoulakis, 1987)*.

6 Conclusions

The Naxos amphibolite boudins offer exciting insights into the evolution of a polyphase boudin system under progressively decreasing temperature and pressure. Most importantly, we measured a thickness control on brittly resolved strain (Figure 6), but could not identify the process(es) compensating for the local strain variation arising from this phenomenon. Our findings also highlight the necessity for characterising such complex systems in 3D, which enabled the presented geometric and mechanical analysis, specifically:

1. Fracture density and failure mode record the progressive cooling and embrittlement of marble and amphibolite during exhumation.
2. Failure mode of brittle boudins varies with layer thickness. Shear fractures are only accommodated in lower aspect ratio swells, while extensional fractures can also localise in pinches.
3. Brittle strain delocalises with decreasing layer thickness. Below the threshold of 10-20 grains thickness, localised fracturing is absent and microscopic deformation bands become constrained to shear zones and necks.
4. No processes accommodating the 'missing' brittle strain could be identified. Presuming the layer stretched homogeneously, the accommodating process remains elusive.
5. The dominant controls on fracture spacing, or boudin width, are structural inheritance, geometric complexity from fracture nucleation, and the effects of failure mode variation. The effect of layer thickness is either occluded by, or exerted through these factors.

7 Acknowledgements

This work was funded by the Deutsche Forschungsgemeinschaft (DFG) as part of the project "BoDy – Boudinage Dynamics" (UR 64/14–1).

8 Figures & Tables

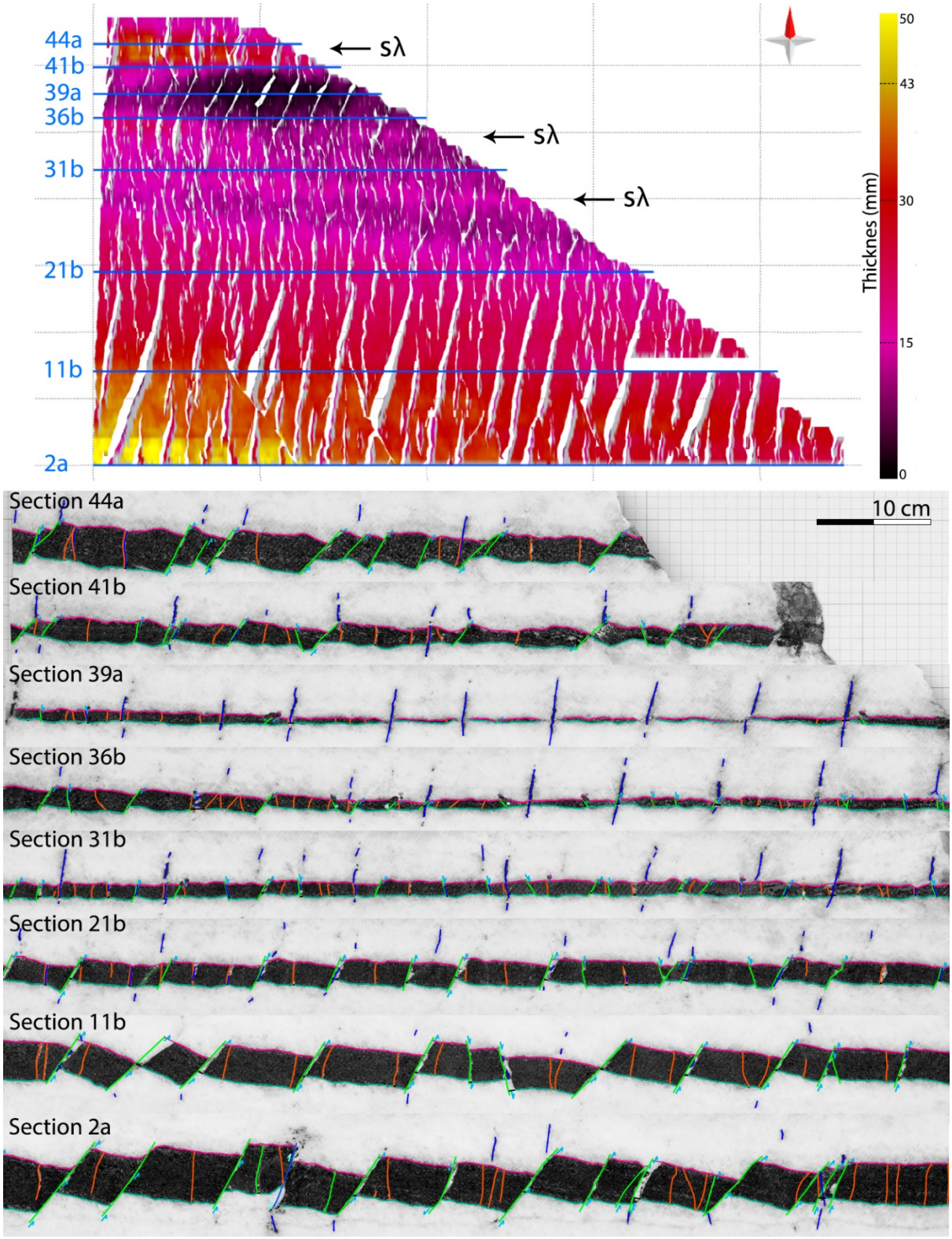

***Figure 1**: The amphibolite layer is characterised by a large-scale thickness gradient from a lλ swell to a lλ pinch (S* to N*) overprinted by sλ swells in the lλ pinch. In sections, closely spaced shear fractures (green), extensional fractures (orange), and chlorite veins (blue) are mapped, and then correlated in 3D (Figure 2). Note the low frequency of shear fractures in sections 31b – 39a and the almost complete lack of layer-confined brittle structures in section 39a.*

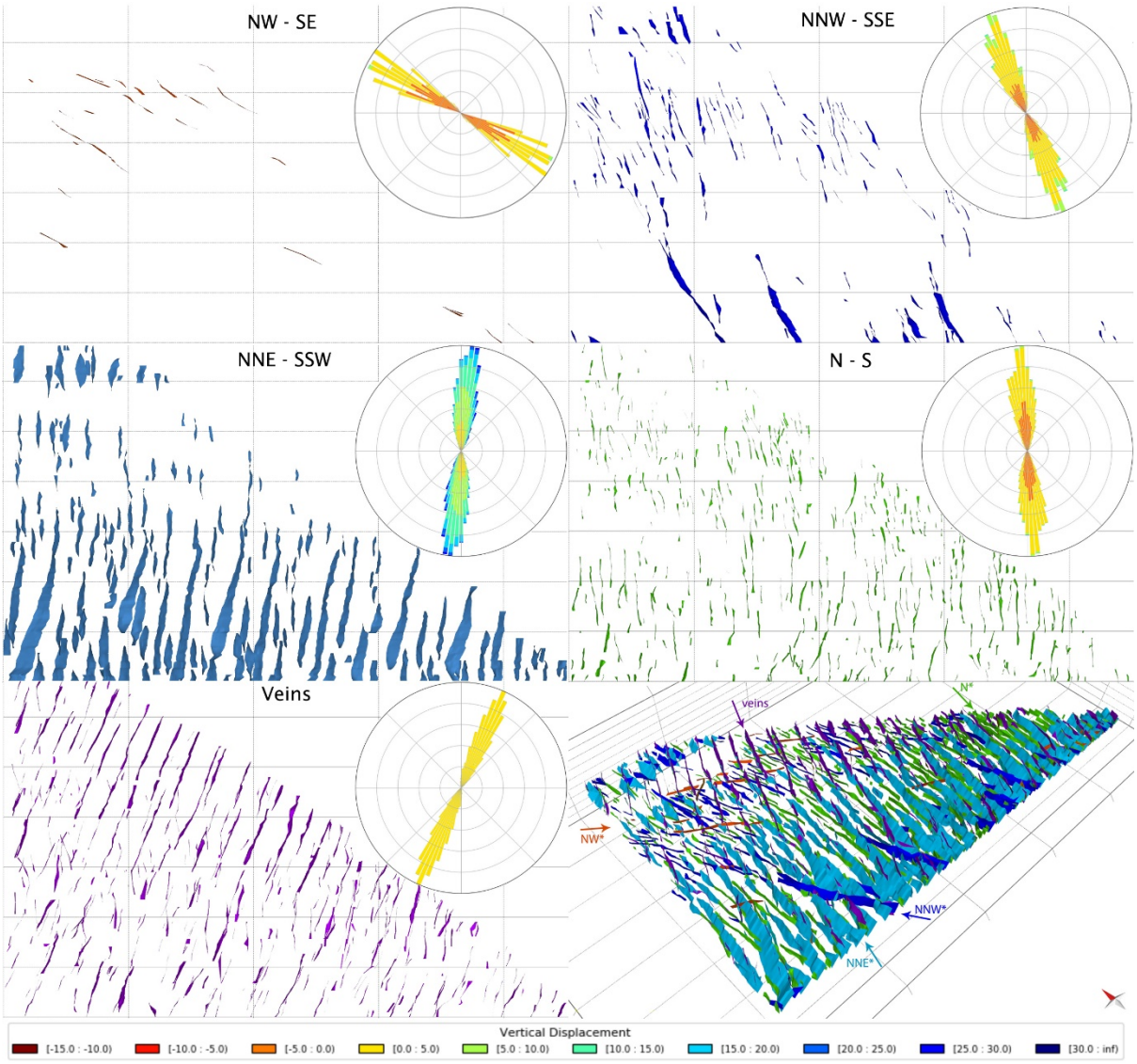

***Figure 2**: Brittle boudinage sets identified in the model (from oldest to youngest: NW*-NNW*-NNE*-N*-Veins) and 3D model of all the fractures. Colour schemes in the rose plots indicate measured throw according to striking direction, as indicated by the legend at the bottom. Grid is 20 × 50 cm.*

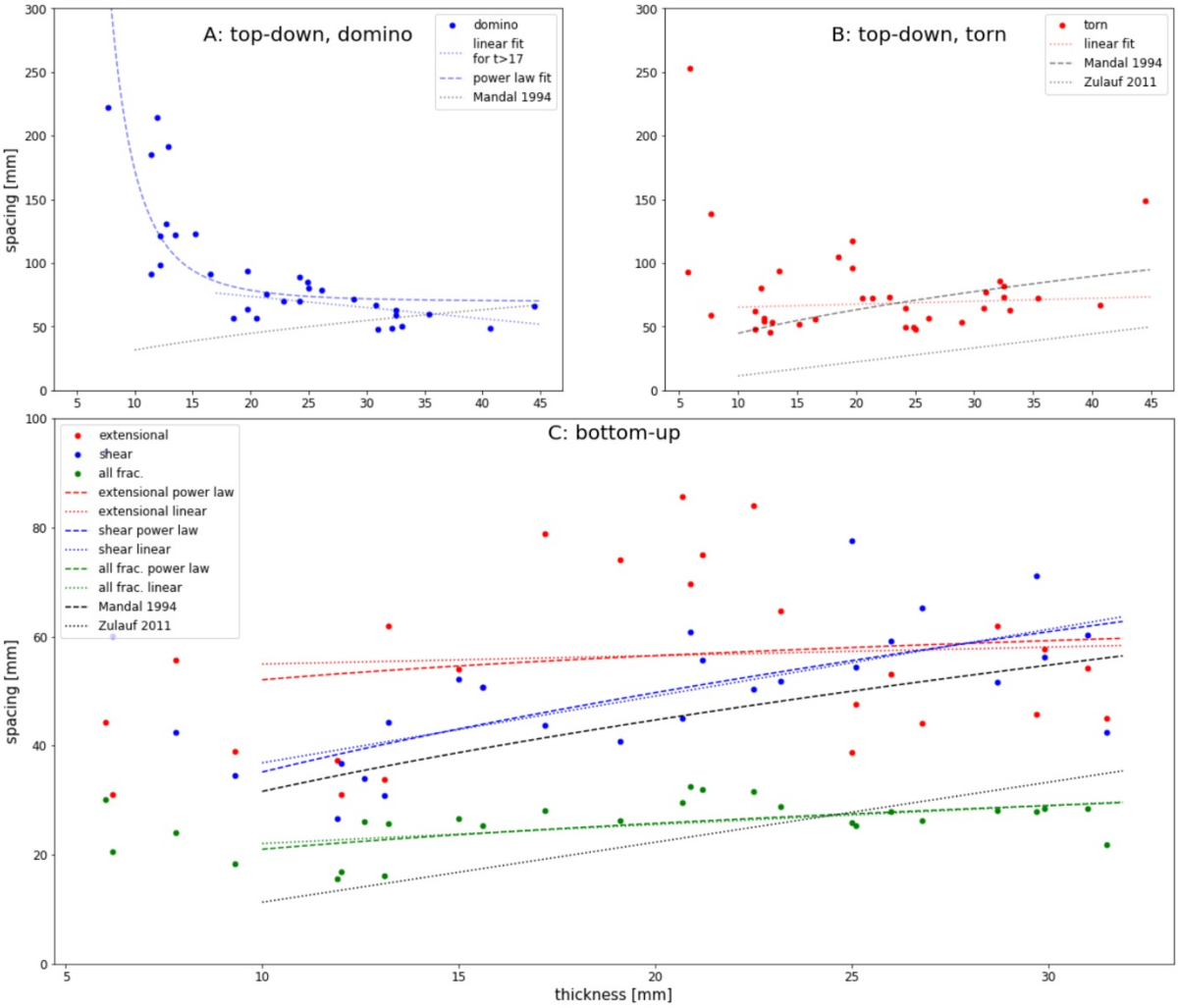

***Figure 3**: (A) Correlation between fracture spacing and layer thickness for individual sets (B) or fracture modes is generally weak and has a high variance. However, calculating spacing for all mapped fractures, regardless of their type, significantly decreases variance. (C) Along the amphibolite layer the N* and NNE* fracture sets (highest fracture density) have a negative correlation, and the dominant set alternates periodically.*

***Table 1**: Fitting parameters for power-law and linear trends to fracture spacing vs thickness data (Figure 3). Top-down approach considers spacing within individual fracture sets, bottom-up approach disregards fracture sets to eliminate biases arising from structural inheritance.*

fit	$a\,t^b$			$mt + i$		
	a	b	R^2	m	i	R^2
top-down						
NNE	977 ± 294.2	-0.8 ± 0.11	0.6		-	
N	35 ± 15.2	0.3 ± 0.14	0.1	1.0 ± 0.51	58 ± 12.1	0.1
bottom-up						
extensional	40 ± 24.3	0.1 ± 0.20	0.02	0.2 ± 0.56	53 ± 12.6	0.004
shear	11 ± 4.7	0.5 ± 0.13	0.4	1.2 ± 0.32	25 ± 7.3	0.4
all fracs	11 ± 3.7	0.3 ± 0.14	0.3	0.3 ± 0.11	10 ± 3.7	0.2

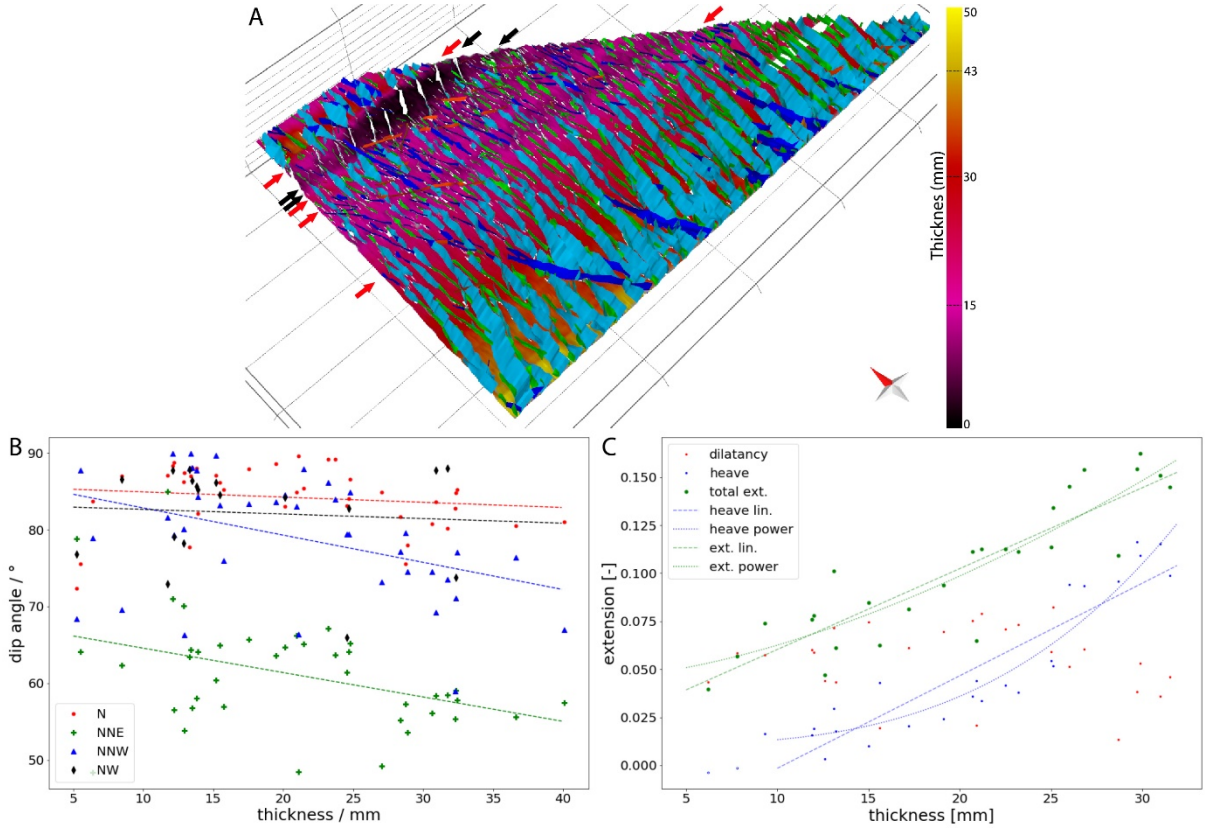

***Figure 4**: (A) Fracture distribution is correlating to layer thickness. Shear fractures are abundant down to a layer thickness of about 20 mm (red arrows) where only extensional fractures remain. Below 10 mm thickness (black arrows), the layer is only disrupted by chlorite veins, layer-confined fractures are absent. Fracture dip of in the shear dominated fracture NNW* & NNE* sets is proportional to layer thickness. The proportionality between fracture dip and thickness is much less pronounced in the extensional fracture dominated NW* & N* sets. Fracture orientation is averaged for each fracture set over sections perpendicular to the thickness gradient. The measured apparent dip angles are converted to true dip. Slopes and intercepts of the fits are: N*: -0.07 ± 0.074, 85 ± 1.7; NNE*: -0.3 ± 0.12, NNW*: -0.4 ± 0.13, 86 ± 2.9; 67 ± 2.7; NW*: -0.06 ± 0.194, 83 ± 3.7. (C) As a consequence of fracture distribution, brittly resolved extension correlates with thickness. The decreasing abundance of shear fractures in thinner amphibolite is recorded in decreasing heave, dilatancy below 10 mm layer thickness is limited to the chlorite veins.*

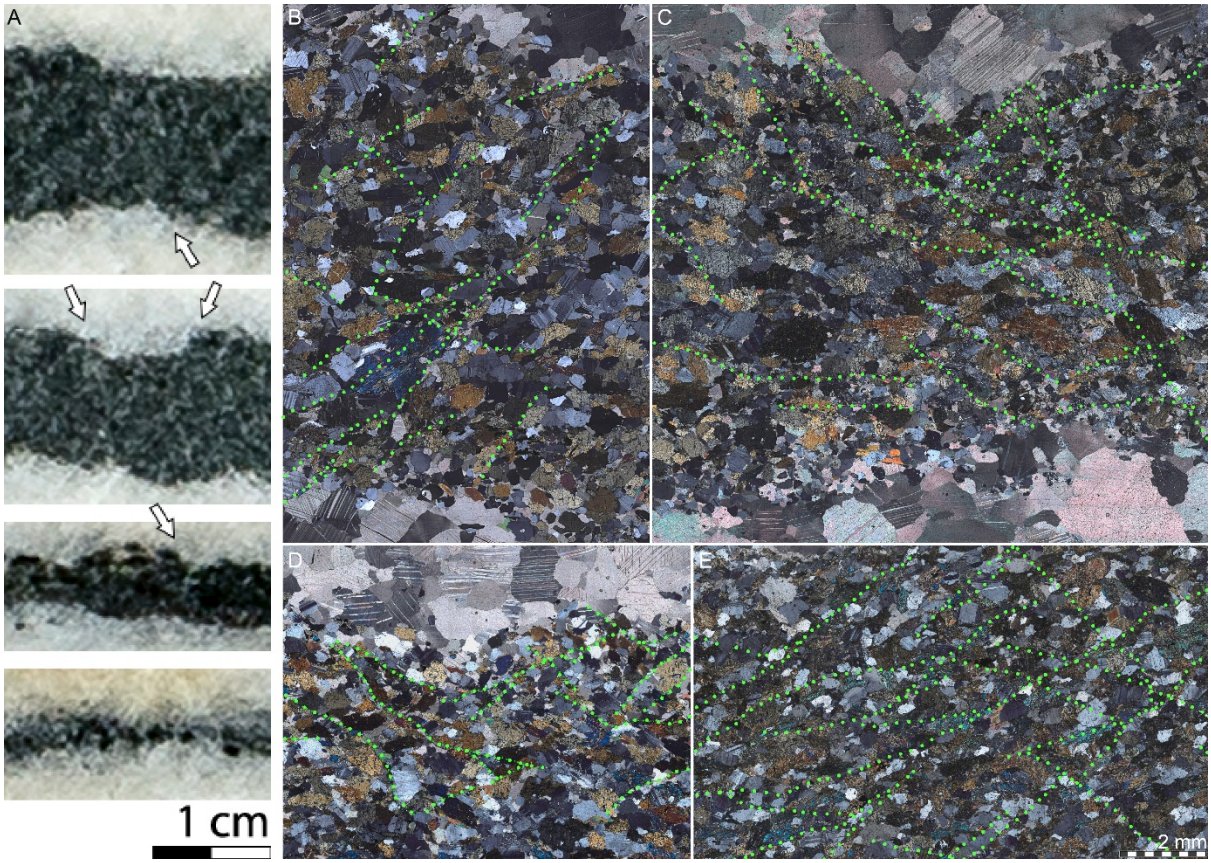

***Figure 5**: (A) Delocalisation in thin amphibolite is progressive, manifesting in necking and wider shear zones just below the thickness threshold for localised fracturing (10 mm), and deformation becomes increasingly more distributed as thickness approaches the grain-scale. (B-E) Micrographs showing of deformation bands in the amphibolite. (B-D) Where the layer is thin (here 7 - 8 mm / 20-30 grains) the bands are clustering in necks and shear zones. (E) In thick amphibolite, the deformation bands are more evenly distributed throughout the entire layer. The scale is identical across all micrographs.*

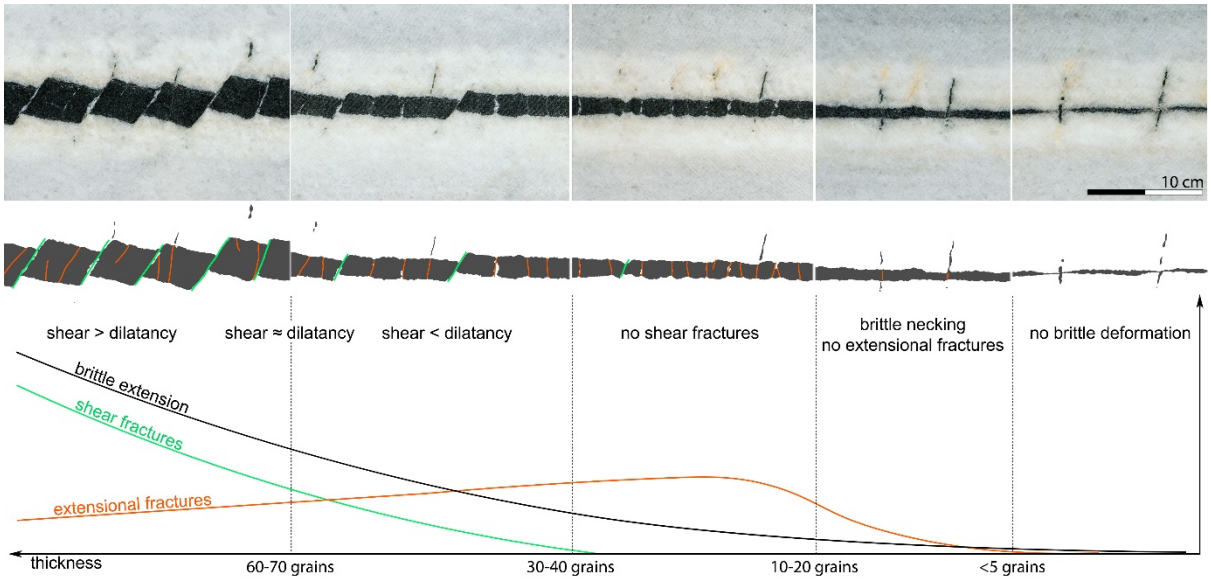

***Figure 6**: The dominant deformation mechanism accommodation extension changes with thickness, which is reflected in measurable brittle extension. This is startling because the amount of strain must be homogeneous throughout the entire sample. In thick layer, shear fractures accommodate most strain, formation of extensional fractures is limited by reactivation of older structures. With decreasing thickness, shear becomes less important and extensional fractures become dominant. Where the layer thins below 10-20 grains thickness, deformation delocalises into extensional necks, where deformation bands are concentrated. Below about 5 grains thickness, no brittle extension can be observed. The mechanisms compensating this localised strain variability remain elusive.*

References

Abe, S. & Urai, J. L. 2012. Discrete Element Modeling of Boudinage: Insights on Rock Rheology, Matrix Flow, and Evolution of Geometry. *Journal of Geophysical Research: Solid Earth,* 117.

Abe, S., Urai, J. L. & Kettermann, M. 2013. Fracture Patterns in Nonplane Strain Boudinage—Insights from 3-D Discrete Element Models. *Journal of Geophysical Research: Solid Earth,* 118**,** 1304-1315.

Bai, T., Pollard, D. & Gao, H. 2000. Explanation for Fracture Spacing in Layered Materials. *Nature,* 403**,** 753-756.

Bai, T. & Pollard, D. D. 2000a. Closely Spaced Fractures in Layered Rocks: Initiation Mechanism and Propagation Kinematics. *Journal of Structural Geology,* 22**,** 1409-1425.

Bai, T. & Pollard, D. D. 2000b. Fracture Spacing in Layered Rocks: A New Explanation Based on the Stress Transition. *Journal of Structural Geology,* 22**,** 43-57.

Buick, I. S. 1991. The Late Alpine Evolution of an Extensional Shear Zone, Naxos, Greece. *Journal of the Geological Society,* 148**,** 93-103.

Fytikas, M., Innocenti, F., Manetti, P., Peccerillo, A., Mazzuoli, R. & Villari, L. 1984. Tertiary to Quaternary Evolution of Volcanism in the Aegean Region. *Geological Society, London, Special Publications,* 17**,** 687-699.

Goscombe, B. D., Passchier, C. W. & Hand, M. 2004. Boudinage Classification: End-Member Boudin Types and Modified Boudin Structures. *Journal of Structural Geology,* 26**,** 739-763.

Jolivet, L. & Brun, J.-P. 2010. Cenozoic Geodynamic Evolution of the Aegean. *International Journal of Earth Sciences,* 99**,** 109-138.

Jolivet, L., Faccenna, C., Huet, B., Labrousse, L., Le Pourhiet, L., Lacombe, O., Lecomte, E., Burov, E., Denele, Y. & Brun, J.-P. 2013. Aegean Tectonics: Strain Localisation, Slab Tearing and Trench Retreat. *Tectonophysics,* 597**,** 1-33.

Jolivet, L., Famin, V., Mehl, C., Parra, T., Aubourg, C., Hébert, R., Philippot, P. & Whitney, D. 2004. Strain Localization During Crustal-Scale Boudinage to Form Extensional Metamorphic Domes in the Aegean Sea. *Special papers-Geological Society of America***,** 185-210.

Kettermann, M. & Urai, J. L. 2015. Changes in Structural Style of Normal Faults Due to Failure Mode Transition: First Results from Excavated Scale Models. *Journal of Structural Geology,* 74**,** 105-116.

Kruckenberg, S. C., Vanderhaeghe, O., Ferré, E. C., Teyssier, C. & Whitney, D. L. 2011. Flow of Partially Molten Crust and the Internal Dynamics of a Migmatite Dome, Naxos, Greece. *Tectonics,* 30.

Lister, G. S., Banga, G. & Feenstra, A. 1984. Metamorphic Core Complexes of Cordilleran Type in the Cyclades, Aegean Sea, Greece. *Geology,* 12**,** 221-225.

Lohest, M. 1909. De L'origine Des Veines Et Des Géodes Des Terrains Primaires De Belgique. *Ann. Soc. Geol. Belgique,* 36**,** 275-282.

Mandal, N., Chakraborty, C. & Samanta, S. K. 2001. Controls on the Failure Mode of Brittle Inclusions Hosted in a Ductile Matrix. *Journal of Structural Geology,* 23**,** 51-66.

Mandal, N., Deb, S. K. & Khan, D. 1994. Evidence for a Non-Linear Relationship between Fracture Spacing and Layer Thickness. *Journal of Structural Geology,* 16**,** 1275-1281.

Marques, F. O., Fonseca, P. D., Lechmann, S., Burg, J.-P., Marques, A. S., Andrade, A. J. & Alves, C. 2012. Boudinage in Nature and Experiment. *Tectonophysics,* 526**,** 88-96.

Mühlhaus, H.-B. & Vardoulakis, I. 1987. The Thickness of Shear Bands in Granular Materials. *Geotechnique,* 37**,** 271-283.

Olson, J. E. 2004. Predicting Fracture Swarms—the Influence of Subcritical Crack Growth and the Crack-Tip Process Zone on Joint Spacing in Rock. *Geological Society, London, Special Publications,* 231**,** 73-88.

Passchier, M., Passchier, C. W., Weismüller, C. & Urai, J. L. 2021. The Joint Sets on the Lilstock Benches, Uk. Observations Based on Mapping a Full Resolution Uav-Based Image. *Journal of Structural Geology,* 147**,** 104332.

Prabhakaran, R., Bertotti, G., Urai, J. & Smeulders, D. 2021a. Investigating Spatial Heterogeneity within Fracture Networks Using Hierarchical Clustering and Graph Distance Metrics. *Solid Earth Discussions***,** 1-42.

Prabhakaran, R., Urai, J. L., Bertotti, G., Weismüller, C. & Smeulders, D. M. 2021b. Large-Scale Natural Fracture Network Patterns: Insights from Automated Mapping in the Lilstock (Bristol Channel) Limestone Outcrops. *Journal of Structural Geology,* 150**,** 104405.

Price, N. J. 1966. *Fault and Joint Development in Brittle and Semi-Brittle Rock,* Oxford, New York, Pergamon Press.

Ramberg, H. 1955. Natural and Experimental Boudinage and Pinch-and-Swell Structures. *The Journal of Geology,* 63**,** 512-526.

Ramsay, A. C. 1881. The Geology of North Wales. *Memoirs of the Geological Survey of England and Wales.* HM Stationery Office.

Ramsay, J. G. 1968. Folding and Fracturing of Rock.

Ramsay, J. G. & Huber, M. I. 1983. *The Techniques of Modern Structural Geology: Strain Analysis*, Academic Press.

Ramsay, J. G. & Huber, M. I. 1987. *The Techniques of Modern Structural Geology: Folds and Fractures*, Academic press.

Schenk, O., Urai, J. L. & Van Der Zee, W. 2007. Evolution of Boudins under Progressively Decreasing Pore Pressure–a Case Study of Pegmatites Enclosed in Marble Deforming at High Grade Metamorphic Conditions, Naxos, Greece. *American Journal of Science,* 307**,** 1009-1033.

Schmalholz, S. M., Schmid, D. W. & Fletcher, R. C. 2008. Evolution of Pinch-and-Swell Structures in a Power-Law Layer. *Journal of Structural Geology,* 30**,** 649-663.

Schöpfer, M. P. J., Arslan, A., Walsh, J. J. & Childs, C. 2011. Reconciliation of Contrasting Theories for Fracture Spacing in Layered Rocks. *Journal of Structural Geology,* 33**,** 551-565.

Schöpfer, M. P. J., Childs, C., Manzocchi, T., Walsh, J. J., Nicol, A. & Grasemann, B. 2017. The Emergence of Asymmetric Normal Fault Systems under Symmetric Boundary Conditions. *Journal of Structural Geology,* 104**,** 159-171.

Schöpfer, M. P. J., Childs, C. & Walsh, J. J. 2007. Two-Dimensional Distinct Element Modeling of the Structure and Growth of Normal Faults in Multilayer Sequences: 2. Impact of Confining Pressure and Strength Contrast on Fault Zone Geometry and Growth. *Journal of Geophysical Research: Solid Earth (1978–2012),* 112.

Schueller, S., Gueydan, F. & Davy, P. 2005. Brittle-Ductile Coupling: Role of Ductile Viscosity on Brittle Fracturing. *Geophysical Research Letters,* 32.

Spruženiece, L., Späth, M., Urai, J. L., Ukar, E., Selzer, M. & Nestler, B. 2021. Wide-Blocky Veins Explained by Dependency of Crystal Growth Rate on Fracture Surface Type: Insights from Phase-Field Modeling. *Geology,* 49**,** 641-646.

Stel, H. 1981. Crystal Growth in Cataclasites: Diagnostic Microstructures and Implications. *Tectonophysics,* 78**,** 585-600.

Urai, J. L., Schuiling, R. D. & Jansen, J. B. H. 1990. Alpine Deformation on Naxos (Greece). *Deformation Mechanisms, Rheology and Tectonics,* 54**,** 509-522.

Vanderhaeghe, O. 2004. Structural Development of the Naxos Migmatite Dome. *Geological Society of America Special Papers,* 380**,** 211-227.

Virgo, S., Abe, S. & Urai, J. L. 2013. Extension Fracture Propagation in Rocks with Veins: Insight into the Crack-Seal Process Using Discrete Element Method Modeling. *Journal of Geophysical Research: Solid Earth,* 118**,** 5236-5251.

Virgo, S., Abe, S. & Urai, J. L. 2014. The Evolution of Crack Seal Vein and Fracture Networks in an Evolving Stress Field: Insights from Discrete Element Models of Fracture Sealing. *Journal of Geophysical Research: Solid Earth,* 119**,** 8708-8727.

Virgo, S., Heup, T., Urai, J. L. & Berlage, T. Virtual Petrography (Vip)-a Virtual Microscope for the Geosciences. EGU General Assembly Conference Abstracts, 2016. 14669.

Virgo, S., Von Hagke, C. & Urai, J. L. 2018. Multiphase Boudinage: A Case Study of Amphibolites in Marble in the Naxos Migmatite Core. *Solid Earth,* 9**,** 91-113.

Von Hagke, C., Bamberg, B., Virgo, S. & Urai, J. L. 2018. Outcrop-Scale Tomography: Insights into the 3d Structure of Multiphase Boudins. *Journal of Structural Geology,* 115**,** 311-317.

Zulauf, J. & Zulauf, G. 2005. Coeval Folding and Boudinage in Four Dimensions. *Journal of Structural Geology,* 27**,** 1061-1068.

Zulauf, J., Zulauf, G., Göttlich, J. & Peinl, M. 2014. Formation of Chocolate-Tablet Boudins: Results from Scaled Analogue Models. *Journal of Structural Geology,* 68**,** 97-111.

Zulauf, J., Zulauf, G. & Hattingen, E. 2020a. Boudinage and Two-Stage Folding of Oblique Single Layers under Coaxial Plane Strain: Layer Rotation around the Axis of No Change (Y). *Journal of Structural Geology,* 135**,** 104023.

Zulauf, J., Zulauf, G. & Hattingen, E. 2020b. Coeval Boudinage and Folding of Oblique Single Layers under Coaxial Plane Strain: Layer Rotation around the Principal Stretching Axis (X). *Journal of Structural Geology,* 141**,** 104217.

Zulauf, J., Zulauf, G., Kraus, R., Gutiérrez-Alonso, G. & Zanella, F. 2011. The Origin of Tablet Boudinage: Results from Experiments Using Power–Law Rock Analogs. *Tectonophysics,* 510**,** 327-336.